



Oxygen vacancies induced special CO₂ adsorption modes on Bi₂MoO₆ for highly selective conversion to CH₄

Xianglong Yang^{a,1}, Shengyao Wang^{a,b,1}, Nan Yang^{a,1}, Wei Zhou^c, Pei Wang^a, Kai Jiang^a, Shu Li^a, Hui Song^{b,d}, Xing Ding^{a,*}, Hao Chen^{a,*}, Jinhua Ye^{b,d,e,**}

^a College of Science, Key Laboratory of Environment Correlative Dietology of Ministry of Education, Huazhong Agricultural University, Wuhan 430070, PR China

^b International Center for Materials Nanoarchitectonics (WPI-MANA), National Institute for Materials Science (NIMS), 1-1 Namiki, Tsukuba, Ibaraki 305-0055, Japan

^c TJU-NIMS International Collaboration Laboratory, School of Materials Science and Engineering, Tianjin University, Tianjin 300072, PR China

^d Graduates School of Chemical Science and Engineering, Hokkaido University, Sapporo 060-0814, Japan

^e TU-NIMS Joint Research Center, School of Materials Science and Engineering, Tianjin 300072, PR China

ARTICLE INFO

Keywords:

CO₂ photoreduction
Oxygen vacancy
Selectivity
Bi₂MoO₆

ABSTRACT

Search for suitable photocatalysts with ultrahigh selective generation of CH₄ from CO₂ is a great challenge in artificial photocatalysis. Herein, effective CO₂ photoconversion to CH₄ with high selectivity up to 96.7% is achieved over oxygen-deficient Bi₂MoO₆ under visible-light. Various characterizations and DFT calculations indicated that well-designed oxygen vacancies (OVs) on the {001} surface of Bi₂MoO₆ can not only enhance light harvesting and e^-/h^+ separation, but favor CO₂ adsorption in a special bidentate carbonate mode, which thermodynamically supports the further hydrogenation of intermediate *CO to generate CH₄. Based on the *in-situ* infrared spectroscopy analysis, the CO₂ adsorption modes and reaction intermediates of two pathways over Bi₂MoO₆ with or without OVs were figured out. The reasonable photocatalytic mechanism for highly selective conversion to CH₄ was also proposed. This work provides new insights to the role of OVs in selective CO₂ photoconversion, and paves ways to design efficient CH₄ evolution systems.

1. Introduction

Artificial photocatalytic conversion of sunlight, CO₂ and H₂O into valuable hydrocarbons, offers a promising strategy for sustainable development and represents a “holy grail” technology for the ultimate goal of solar energy conversion [1–3]. Unfortunately, CO₂ photoconversion is far from the practical implementation as high energy input is required for the dissociation of C=O (~750 kJ mol⁻¹) in CO₂ molecules [4,5]. With tremendous endeavors of researchers, numerous heterogeneous photocatalysts have been developed to be active for CO₂ photoreduction till now [6–10]. Due to the lack of highly selective active sites, most of them still suffer from fairly poor selectivity towards the desired hydrocarbons, especially the high value-added CH₄, and also highly rely on the addition of exogenous metal sites as cocatalysts, which prefer to provide desirable electron-proton coupling for the CH₄ photogeneration [11]. Hence, on the basis of surface reaction control mechanisms for CO₂ photoreduction, the strategies of

nanoarchitectonics aiming to construct the reliable active sites and to boost the selective reactions are desperately needed [12–16].

Among the reported various approaches, defect engineering, especially the introduction of oxygen vacancies (OVs), has caught great attentions recently, since it was certified as a remarkable method to engineer the band gap and tailor the electronic structures of oxide semiconductors [17,18]. Generally, OVs can effectively extend the photoresponse to visible/IR light region, owing to the formation of OV-induced defect states below the conduction band [19,20]. Moreover, the existence of defect states can also effectively trap charge carriers, hence accelerating the separation of photogenerated electron-hole pairs [21,22]. Most importantly, OVs with abundant localized electrons are natural active site for the enhanced adsorption and activation of inert gas molecules and of particular interests for promoting the electron-proton coupling reaction [23–25]. Especially for the CO₂ photoreduction, the OVs introduced on semiconductors can not only strengthen the CO₂ chemical adsorption, but also act as active site for indirectly

* Corresponding authors at: International Center for Materials Nanoarchitectonics (WPI-MANA), National Institute for Materials Science (NIMS), 1-1 Namiki, Tsukuba, Ibaraki 305-0055, Japan.

** Corresponding author.

E-mail addresses: dingx@mail.hzau.edu.cn (X. Ding), hchenhao@mail.hzau.edu.cn (H. Chen), jinhua.YE@nims.go.jp (J. Ye).

¹ These authors contributed equally to this work.

activating CO_2 to C^+O_2^- , which is identified as the rate-limiting step for CO_2 photoreduction [26]. In this case, various photocatalysts including Bi_2MoO_6 with OV have been reported with activities for CO_2 photoconversion [27]. However, most researches mainly focus on the enhancement of photocatalytic activities, while the corresponding selectivity has rarely been discussed, let alone the investigations of correlations between OVs and selective CO_2 conversion [28–30]. Therefore, it is of great significance and importance to unearth a model oxygen-deficient semiconductor to disclose the potential role of OVs in selective CO_2 photoreduction.

As a typical Aurivillius oxides, Bi_2MoO_6 is sought-after and regarded as a promising visible-light-responsive photocatalysts, by virtue of its intrinsic chemical inertness, appropriate band potentials, and unique layered structure [31,32]. Be constructed by alternating $[\text{Bi}_2\text{O}_2]^{2+}$ layers and perovskite-like $[\text{MoO}_4]^{2-}$ slabs with oxygen atoms bridged between layers, Bi_2MoO_6 possess exceptional characteristic of facile OVs generation under O_2 -deficient thermal conditions because of the low energy of surface Bi-O bonds [18,33–35]. By now, various defective Bi_2MoO_6 -based catalysts have been synthesized and utilized in environmental remediation and renewable energy production [32,36,37]. For instance, Atomically-thin Bi_2MoO_6 nanosheets with surface “Bi-O” vacancy pairs, fabricated by virtue of ultrathin BiOCl , possessed fantastic activity for CO evolution [29]. OVs concentration tunable Bi_2MoO_6 , synthesized by the tetramethylethylenediamine-assisted solvothermal method, exhibited efficient photocatalytic decomposition of ciprofloxacin [36]. In our previous work, Bi_2MoO_6 was observed to prefers to transfer the photogenerated excitons in the layer paralleling to the [001] direction of it and thus exhibited excellent performance on photocatalytic oxidation of nitric oxide [38]. Inspired by these fantastic properties of Bi_2MoO_6 , we speculated that the Bi_2MoO_6 with {001} facets exposed might be an ideal platform for providing atomic level insights into the impacts of OVs on the selective CO_2 photoconversion.

Bearing these aspects in mind, we chose the Bi_2MoO_6 with {001} facets exposed as the model materials to explore the CO_2 adsorption modes and the reaction process, which is the first report about unveiling the hidden mechanism for CO_2 selective conversion over OVs. The density functional theory (DFT) calculations was first carried out to predict the impact of OVs on CO_2 adsorption and photocatalytic reduction pathway on the surface of Bi_2MoO_6 . Under the enlightenment of theoretic calculation, we synthesized {001} facets exposed Bi_2MoO_6 with OVs via a facial solvothermal approach and applied characterizations to confirm the existence of OVs on Bi_2MoO_6 . After further performed the influence of OVs on the photoelectrochemical property of Bi_2MoO_6 , the correlations between OVs and selectivity in CO_2 photoreduction under visible light irradiation were investigated by comparing and analyzing the products generated over Bi_2MoO_6 (BMO) and oxygen deficient Bi_2MoO_6 (BMO-OVs). Benefiting from the existence of OVs on the surface of Bi_2MoO_6 and the consequent natural-active-sites with high selectivity for CO_2 photoconversion, the present BMO-OVs exhibits extraordinary high selectivity and stability for CH_4 photo-generation. More importantly, this study provides new insights to the role of OVs in selective CO_2 photoconversion, and paves new pathways for designing advanced efficient photocatalytic CH_4 evolution systems under visible light irradiation.

2. Experimental section

2.1. Chemicals and materials

All reagents used were of analytical grade and used without further purification. The Bi_2MoO_6 with OVs was prepared via a highly facile one-step ethylene glycol-assisted solvothermal process. Typically, 5 mmol $\text{Na}_2\text{MoO}_4 \cdot 2\text{H}_2\text{O}$ was added slowly into 75 mL ethylene glycol solution containing a stoichiometric amount of $\text{Bi}(\text{NO}_3)_3 \cdot 5\text{H}_2\text{O}$. The resulting mixture was then poured into a 100 mL Teflon-lined stainless autoclave and reacted for 12 h at 140 °C. After cooling the autoclave to

room temperature in air, the resultant precipitate was filtered, washed consecutively with deionized water and ethanol to remove residual ions. The final product was dried at 80 °C in air and denoted as BMO-OVs for further use. The corresponding defect-free Bi_2MoO_6 was synthesized by calcining BMO-OVs at 450 °C in the air for 5 h to reoxidize the surface and was denoted as BMO. For comparison, samples synthesized with ethylene glycol-assisted solvothermal process at different temperatures (130, 140, 150 or 160 °C) were designated as BMO-X (X = 130, 140, 150, 160).

2.2. Characterizations

The X-ray diffraction (XRD) patterns of the samples were obtained using a Bruker D8 Advance X-ray diffractometer with $\text{K}\alpha$ radiation ($\lambda = 1.5418 \text{ nm}$). Raman spectra were acquired on a DXR Raman Microscope (Thermo Fisher, USA). Fourier transform infrared spectra (FT-IR) were recorded on a Nicolet iS50 FT-IR spectrometer (Thermo Fisher, USA). Electron paramagnetic resonance (EPR) spectra were obtained using a Bruker EMX EPR Spectrometer. Oxygen vacancy concentration was determined by referencing to the spin numbers of lone electrons of the Cr(III) in MgO calibration, which is a stable and highly sensitive material to EPR [36]. The morphologies and microstructures of the prepared samples were analyzed via Field-emission scanning electron microscopy (FESEM, FEI-400F, USA) and transmission electron microscopy (TEM, JEOL JEM-2010, Japan). High-resolution transmission electron microscopy (HRTEM) imaging was carried out on a Tecnai G2 F20 S-TWIN microscope (FEI, USA) operated at 200 kV. The surface electronic states of the samples were analyzed via X-ray photoelectron spectroscopy (XPS, ESCALAB 250Xi, USA), and all binding energies were referenced to the C 1s peak at 284.6 eV of the surface adventitious carbon. Brunauer-Emmett-Teller (BET) specific surface area was estimated on a nitrogen adsorption-desorption apparatus (ASAP 2040, Micrometrics Inc., USA) with all samples degassed at 120 °C for 12 h prior to measurements. Temperature programmed desorption (TPD) measurements were carried out on Micrometrics TriStar II 3020. UV-vis diffuse reflectance spectra (DRS) were obtained using a Shimadzu UV-3100 recording spectrophotometer. The photoluminescence (PL) measurements were conducted on a fluorescence spectrometer (LS55, PerkinElmer, USA) using 325 nm as excitation wavelength.

2.3. Measurement of photocatalytic activity

Generally, CO_2 photoconversion is carried out in the liquid or gas phase system. For the liquid system, catalysts can be dispersed uniformly and well attached with the dissolved CO_2 species such as CO_3^{2-} , HCO_3^- and H_2CO_3 , thus it has been adopted in a lot of research. Nevertheless, limited by the competition with water splitting reaction and the difficulties in products separation, the conversion efficiency towards desired hydrocarbons, especially high value-added CH_4 , is still low in liquid system. Herein, the photocatalytic reduction of CO_2 was operated in a 500 mL homemade gas-closed system at ambient temperature and atmospheric pressure. Typically, 50 mg catalyst was uniformly dispersed onto the watch-glass, which was then put in the reaction cell A 300 W Xe-lamp (PLS SXE300, Beijing Perfectlight Inc., China) with a UV-cutoff filter ($\lambda \geq 420 \text{ nm}$) was used as a light source. Prior to the light irradiation, the reactor was sealed and vacuum-treated to completely remove air. CO_2 and H_2O vapor were obtained from the reaction of 1.5 g NaHCO_3 and 5.0 mL 4.0 M H_2SO_4 solution (injected into the reactor after the vacuum treatment). During the irradiation, 2 mL gas was taken from the reactor at regular intervals (1 h) via a syringe and analyzed using a gas chromatograph (SP-7820, TDX-01 column, Rainbow chemical instrument Co. Ltd., China) equipped with a flame ionized detector (FID) and methanizer. The sample gases were calibrated with a standard gas mixture and determined through the retention time. The stability of the sample was evaluated through

recycling photoreduction of CO₂ over BMO-OVs under the same circumstance. After each reaction, the photocatalyst was collected, dried, and then used for the next run. The corresponding overall activity for the CO/CH₄ generation can be evaluated with total consumed electron number (TCEN), which is calculated by Eq. (1).

$$\text{TCEN} = \frac{2 \times (c_{\text{CO}} + 4c_{\text{CH}_4}) \times V_{\text{reactor}}}{m_{\text{cat}} \times t_{\text{irr}}}$$

Where, TCEN is the total consumed electron number for the CO/CH₄ generation. c_{CO} and c_{CH_4} are the produced CO and CH₄ concentration, respectively. V_{reactor} is the reactor volume. m_{cat} is the catalyst mass. t_{irr} is the irradiation time.

2.4. In situ DRIFTS analyses for CO₂ photoreduction

In situ DRIFTS (diffuse reflectance infrared Fourier transform spectra) tests were conducted on Nicolet iS50FT-IR spectrometer (Thermo Fisher, USA) equipped with a designed reaction cell and a liquid nitrogen cooled HgCdTe (MCT) detector. Typically, the substrate lying in the center of the cell was pre-deposited with a thin layer of the sample film. Then each sample was purged with Ar (50 mL/min) for 1 h at 120 °C to blow out all the gases in the cell and adsorbed on the samples. After the reaction cell cooling down to 30 °C, the mixture of CO₂ (5 mL/min), Ar (25 mL/min) and a trace of H₂O vapor were introduced into the reactor for about 30 min to ensure sorption equilibrium before irradiation. The IR signal was in situ collected through a MCT detector along with the reaction.

3. Results and discussion

3.1. Theoretical calculation analysis

DFT calculations were firstly conducted to compare the band structures and total density of states of BMO and BMO-OVs. The typical crystal structure of orthorhombic Bi₂MoO₆ was shown in Fig. S1a and 1b, by contrast, the model of OV decorated Bi₂MoO₆ was built by removing an oxygen atom from the primitive cell (Fig. S1c). Obviously, a new intermediate band mainly composed of Bi 6p appeared in the energy gap of BMO-OVs (Fig. 1a and S1d), implying the formation of defect level, which might favor the electron excitation and e^-/h^+ separation of Bi₂MoO₆ [19]. Besides, DFT calculations were also conducted to predict the impact of OV on CO₂ adsorption over Bi₂MoO₆. The adsorption energies of CO₂ on BMO and BMO-OVs with different adsorption modes were calculated and compared in Fig. S2, from which CO₂ adsorbed with bend mode on both BMO and BMO-OVs was found to be the most favorable configuration as compared with linear mode [39]. In detail, the CO₂ molecules preferred to bound to the BMO-OVs surface through the C atom with a surface O site and through the two self-O atoms that were bound to the two surface Bi centers (B1–CO₂), which resulted in B1–CO₂ with $\Delta E_{\text{ads}} = -0.47$ eV. As for the BMO, the CO₂ molecules tended to bond to its surface adjacent O and single Bi atom (B2–CO₂), which resulted in B2–CO₂ with $\Delta E_{\text{ads}} = -0.39$ eV. Moreover, the charge density difference calculation further revealed the OV is more beneficial for CO₂ chemical adsorption (Fig. 1b and c). After CO₂ was adsorbed on the BMO-OVs surface, 0.15 electrons back-donation from the slab to the B1–CO₂ occurred, which was depicted by the localized electrons depletion on two Bi atoms around the oxygen vacancy and electrons accumulation on the B1–CO₂. Whereas for B2C–O₂ on the BMO surface, 0.07 electrons transferred from CO₂ to slab on the contrary. Additionally, in comparison with that of dissociative CO₂ molecule (1.18 Å), the C–O bonds length of absorbed CO₂ obviously increased to 1.26 Å or 1.29 Å for BMO-OVs and 1.26 Å or 1.30 Å for BMO, respectively. All these results demonstrated that the OV on Bi₂MoO₆ {001} surface facilitated the formation of more stable state of B1–CO₂ and promote different activation level, which might alter the CO₂ conversion pathway and realize the high selectivity of CO₂

photoreduction over Bi₂MoO₆.

A broader DFT study was thus performed to further explore the possible CO₂ conversion pathways and intermediate species initiated by these two different CO₂ adsorption configurations (Fig. 1d and e). Specifically, the B1–CO₂ and B2C–O₂ were initially hydrogenated to produce *COOH, which was subsequently converted to *CO and *OH. Whereafter, the *OH transformed into H₂O, while *CO would be desorbed from the surface immediately with formation of CO (Pathway I) or further hydrogenated to generate *CHO (Pathway II), a prerequisite for the subsequent hydrogenation processes to generate CH₄ ultimately [40]. Notably, the energies of *CO transformation varied with different Bi₂MoO₆ surface. For BMO-OVs, both the hydrogenation and desorption of *CO were favorable processes, but the energy release of the former (3.26 eV) was much higher than that of the latter (0.53 eV), thereby implying Pathway II was more thermodynamically accessible than the Pathway I. As for the BMO, the desorption of *CO was thermodynamically favorable with 0.63 eV of energy emission while the hydrogenation of *CO need 0.75 eV of energy expenditure, demonstrating CO₂ was more probably reduced to CO going through Pathway I rather than Pathway II. To better understand the CO₂ conversion pathways over Bi₂MoO₆ with or without OVs, the further hydrogenation processes of *CHO to produce CH₄ were also simulated (Fig. S3) [41,42]. Once *CHO came into being, it would like to be stepwisely converted into *CHOH, *CH₂OH, *CH₃OH and the final product CH₄. It's worth noting that although the continuous hydrogenation processes of *CHO are endothermic reactions, consistent with previous reports [22,40,42], the conversion of *CHO to CH₄ on BMO-OVs is more thermodynamically favorable than that on BMO based on the corresponding energy expenditure in each step. Integrating all of the results, the introduction of OVs on the prototypical {001} surface of Bi₂MoO₆ might be a viable strategy for selective CO₂ conversion, since OVs can favor the CO₂ absorption in a possible special B1–CO₂ mode, which thermodynamically supports the further hydrogenation of intermediate CO* with the formation of *CHO, which was finally converted into CH₄ after series of subsequent hydrogenation steps.

3.2. Identification of OVs

Motivated by the theoretical calculation results above, we then synthesized {001} facet exposed Bi₂MoO₆ with or without OVs through a facile method. The crystallographic structure and phase purity of the prepared catalysts were investigated by X-ray diffraction (XRD) and Raman spectra analysis. All the XRD patterns (Fig. 2a and S4a) could be readily indexed to the orthorhombic phase Bi₂MoO₆ (JCPDS No. 21-0102). From the Raman spectra, well defined phonon modes were observed in the 200–1200 cm^{−1} wavenumber range, corresponding to the stretching vibrations and bending motions of vibrational modes of Bi₂MoO₆ (Fig. 2b and S4b) [43]. Compared with BMO, BMO-OVs exhibited much weaker and broader Raman signal, consistent with the XRD analysis, indicating the smaller crystallite size and poorer crystallinity of them. Notably, peak at 138 cm^{−1} in BMO corresponding to the lattice motions of [Bi₂O₂]²⁺ shifted to 155 cm^{−1} in BMO-OVs (inset of Fig. 2b), which should be ascribed to the partial oxygen loss in Bi–O bonds [44]. Field emission scanning electron microscopy (FE-SEM) imaging revealed that both BMO-OVs and BMO are composed of hierarchical microspheres assembled from radically grown nanosheets, and BMO sphere was a little denser than BMO-OVs due to the continuous crystallization in the heat treatment with oxygen (inset of Fig. 2c and d). From the high-resolution transmission electron microscopy (HR-TEM) images, both of them were observed to have legible orthorhombic lattice fringes with spaces of 0.274 nm and 0.270 nm (Fig. 2c and d), respectively ascribed to the (200) and (060) planes of orthorhombic Bi₂MoO₆, thereby suggesting both of them are indeed exposed with the {001} facets [38].

The OV generation on Bi₂MoO₆ was initially confirmed via EPR measurement (Fig. 2e and S6). As expected, characteristic OV signals

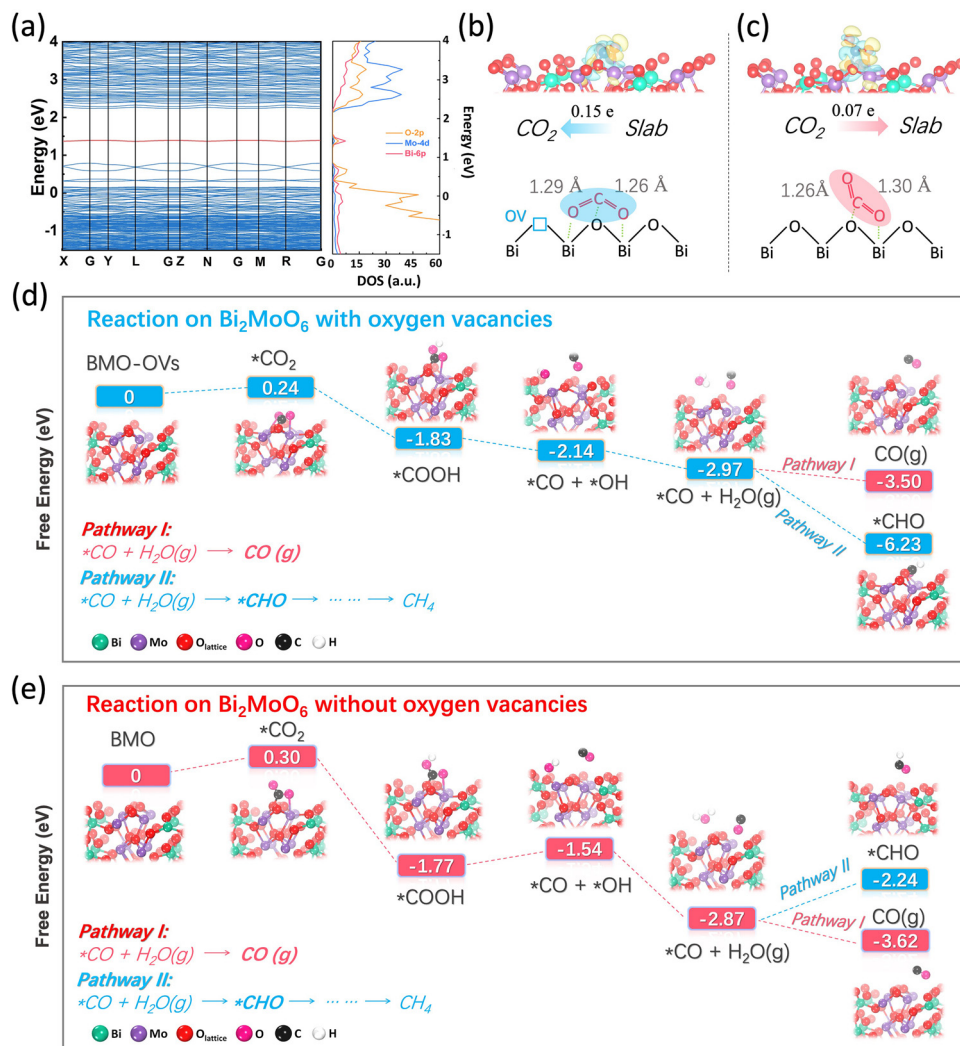


Fig. 1. (a) Calculated band structures and total density of states (DOS) of BMO-OVs. Absorption of B1–CO₂ on BMO-OVs (b) and B2–CO₂ on BMO (c). The yellow and blue isosurfaces with an isovalue of 0.003 au represent charge accumulation and depletion in the space. Reaction pathways for CO₂ reduction on BMO-OVs (d) and BMO (e). “*” represents adsorption on substrate (For interpretation of the references to colour in this figure legend, the reader is referred to the web version of this article).

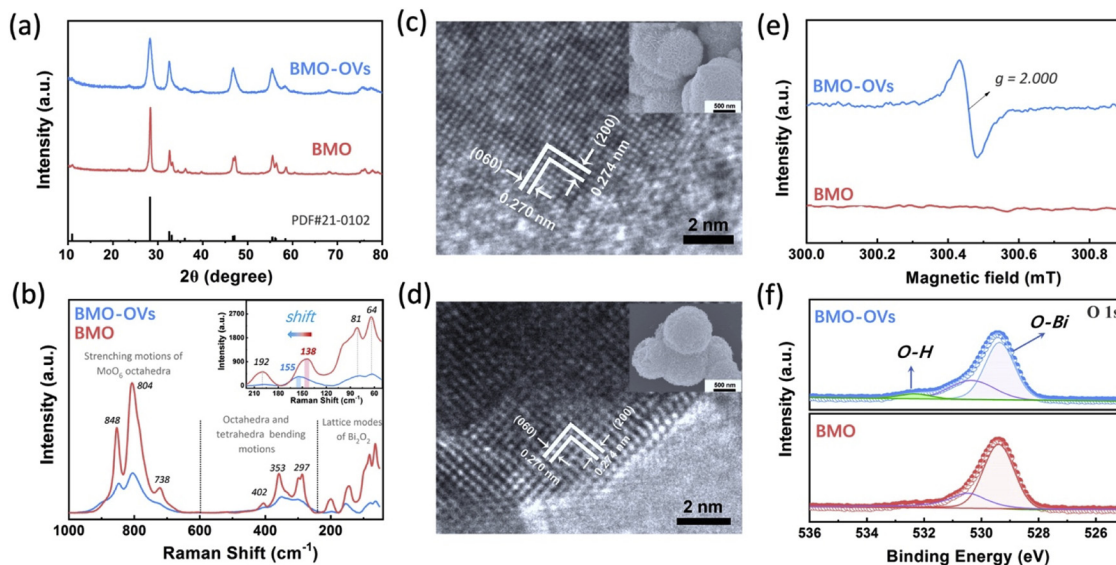


Fig. 2. (a) XRD patterns; (b) Raman spectra; HRTEM and FESEM (inset) images of BMO-OVs (c) and BMO (d); (e) ESR spectra and (f) O 1s XPS spectra of BMO-OVs and BMO.

at $g = 2.000$ were observed for all the solvothermal synthesized catalysts, signifying the successful OVs generation on Bi_2MoO_6 . And the oxygen vacancy concentrations increased gradually as the solvothermal temperature rose from 130 °C to 160 °C. For further confirmation, X-ray photoelectron spectroscopy (XPS) analysis was thus performed to analyze the chemical states of materials. The XPS survey spectra of BMO-OVs and BMO illustrated the prepared samples were composed of Bi, Mo, O and a trace amount of C (Fig. S7a). In the high-resolution XPS spectra of Bi 4f and Mo 3d regions, the peaks centered at 158.7, 164.0, 231.9, and 235.1 eV are attributed to the Bi 4f_{7/2}, Bi 4f_{5/2}, Mo 3d_{5/2}, and Mo 3d_{3/2}, respectively (Fig. S7b and S7c) [45]. All of them showed a slight shift to the lower binding energy in BMO-OVs, which resulted from the chemical environment changes due to the departure of partial oxygen atoms. With respect to O 1s spectra (Fig. 2f), the relative intensity of the peak at 529.0 eV corresponding to Bi-O bond in BMO-OVs was much weaker than that in BMO, implying the partial loss of O atoms connected with Bi atoms under the solvothermal condition. Meanwhile, an additional peak at 532.2 eV, attributed to O-H bond, appeared in the O 1s spectrum of BMO-OVs, which should be indexed to the surface hydroxyl or H_2O . This result was further verified via the FT-IR spectra (Fig. S8), where the emerging peaks at $\sim 3450\text{ cm}^{-1}$ and $\sim 1625\text{ cm}^{-1}$ corresponded to stretching vibrations and bending vibrations of surface -OH, respectively. In the C 1s spectra regions, peaks at 284.8, 286.0, and 287.8 eV were ascribed to the contaminant C, C=O and COR(H) groups, respectively (Fig. S7d) [46]. Interestingly, the relative peak intensity at 286.0 eV in BMO-OVs was much higher than that in BMO, which arose from the enhanced surface adsorption of CO_2 on OVs. According to above results, we inferred that OVs were successfully introduced into the {001} exposed Bi_2MoO_6 microspheres by the synthetic method. In addition, the adsorption of H_2O and CO_2 on the surface of Bi_2MoO_6 was significantly strengthened with the introducing of OVs, which could provide a more convenient environment for CO_2 photoconversion.

3.3. Photoelectrochemical properties

The UV-vis absorption of the materials was further evaluated in Fig. 3a. BMO-OVs exhibited a much intense continuous absorption than that of BMO over the Vis-NIR region, which could be attributed to the

occurrence of OVs-induced sub-band excitation from defect states to CB. Based on the Kubelka-Munk equation, the band gap energies (E_g) of BMO-OVs and BMO were calculated to be 2.55 and 2.63 eV, respectively (inset of Fig. 3a). Further, the Mott-Schottky (MS) plot and valence-band XPS (VB-XPS) spectra were employed to pinpoint their band positions. The flat band potentials of BMO-OVs and BMO were estimated to be 0.13 and 0.37 V versus the Ag/AgCl electrode from the MS plots (Fig. S9), which were equal to 0.74 and 0.98 V versus the Normal Hydrogen Electrode (NHE), respectively. The VB-XPS spectra in Fig. 3b demonstrated that the energy gap between Fermi level (E_f) and VB were 1.53 and 1.28 eV for BMO-OVs and BMO. Since the flat band potential of n-type semiconductor equals to the Fermi level, their VB positions were calculated to be 2.27 and 2.26 V, respectively [38,47]. Combining with the band gaps, their CB positions were determined to be -0.28 and -0.37 V, negative than E_0 ($\text{CO}_2/\text{CO} = -0.11\text{ V}$ vs NHE) and E_1 ($\text{CO}_2/\text{CH}_4 = 0.17\text{ V}$ vs NHE), suggesting the possibility of CO_2 photo-reduction over Bi_2MoO_6 . The respective data are summarized in Table S1 and Fig. 3c. The photoluminescence emission, mainly resulting from the recombination of excited electrons and holes, was displayed in Fig. S10. At the excitation wavelength of 325 nm, the intensity of BMO-OVs was much lower than that of defect-free BMO, which suggested that the charge recombination rate was greatly suppressed due to the presence of OVs. Meanwhile, the photocurrent response spectra and electrochemical impedance spectra, reflecting the charge transfer efficiency, were displayed in Fig. 3d and e. As expected, BMO-OVs exhibited a higher photocurrent and a smaller semicircle diameter than BMO, corresponding to the enhanced separation efficiency and mobility of photoinduced carriers. As a consequence, more electrons and holes may participate in the catalytic reaction and improve the photocatalytic performance of Bi_2MoO_6 .

3.4. Selective CO_2 photoconversion

The selective photocatalytic reduction performance of CO_2 over BMO and BMO-OVs was thus evaluated and compared through solid-gas interface reaction in the gaseous system using H_2O vapor without any sacrificial agent under visible light irradiation (Fig. 4a). Control experiments shown in Fig. S11 revealed that both the photocatalyst and irradiation are necessary and CO_2 can be reduced to CO and CH_4 in the

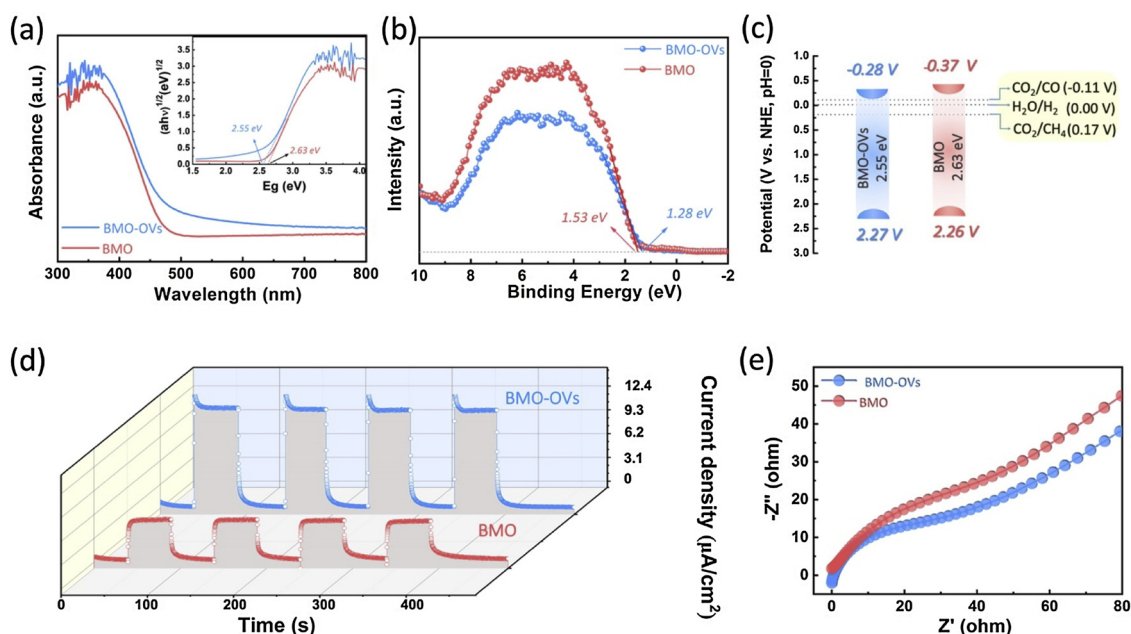


Fig. 3. (a) UV-vis absorption spectra and the plots of $(ah\nu)^{1/2}$ versus $h\nu$ (inset), (b) valence-band XPS (VB-XPS) spectra, (c) the diagram of band positions, (d) photocurrent response spectra and (e) electrochemical impedance spectra (EIS) of BMO-OVs and BMO.

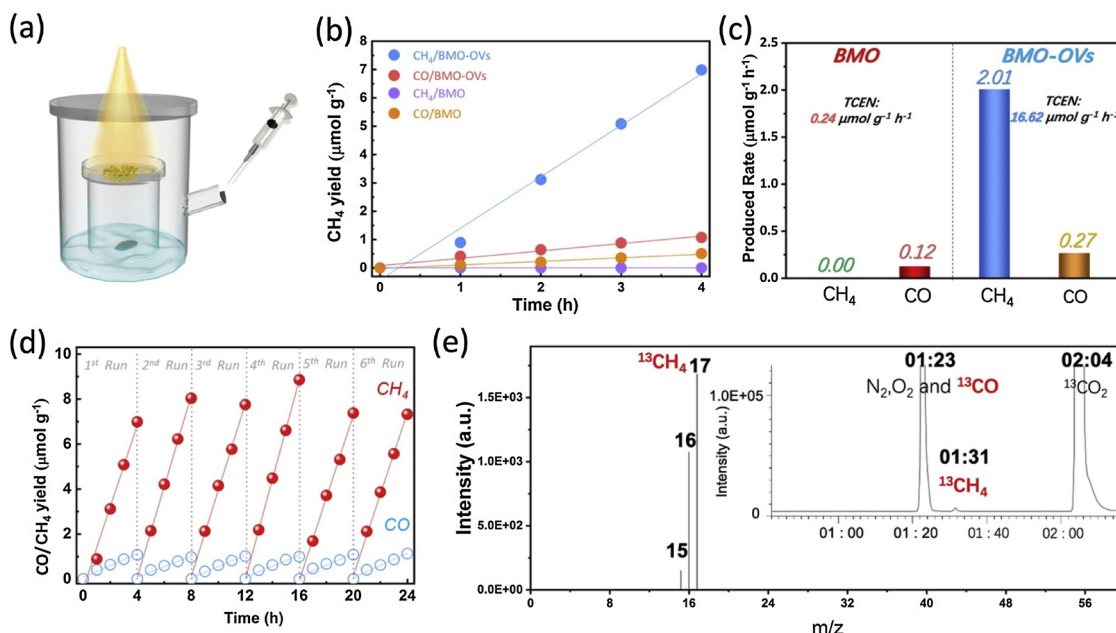


Fig. 4. (a) Schematic illustration of the cell for CO₂ photoconversion; (b, c) CO and CH₄ production and the TCEN value for CO₂ photoreduction over the BMO-OVs and BMO during 4 h visible-light irradiation; (d) typical time course of the amount of CO/CH₄ generated over BMO-OVs under visible-light irradiation; (e) the mass spectra of methane generated under ¹³CO₂ atmosphere, the inset shows the gas chromatogram observed during long-term irradiation under ¹³CO₂ atmosphere.

presence of H₂O vapor. It is noteworthy that the defect-free BMO only showed a production rates of CO (0.12 μmol g⁻¹ h⁻¹) with overall photoactivity (TCEN) of 0.24 μmol g⁻¹ h⁻¹ (Fig. 4b and c). But for BMO-OVs, with the introduced OVVs serving as the natural active sites, remarkable CH₄ generated (2.01 μmol g⁻¹ h⁻¹) as the main product besides of CO (0.27 μmol g⁻¹ h⁻¹) with fairly high TCEN of 16.62 μmol g⁻¹ h⁻¹, which has been rarely reported in bismuth based photocatalytic systems (Table S2). In addition, we also compared the evolution of CO and CH₄ over Bi₂MoO₆ with different amount of OVVs during the 4 h irradiation, which was synthesized at different temperature (Fig. S12 and S13). All oxygen-deficient Bi₂MoO₆ samples exhibited obvious generation of CH₄ under visible light irradiation. The CO and CH₄ evolution rate, especially the CH₄ generation rate was found to show an obvious increasing trend when the solvothermal temperature increased from 130 to 140 °C while further heating-up led to a significant decrease in the overall activity (TCEN), which should be ascribed to the existence of excessive OVVs serving as the recombination centers for charge carriers. To evaluate the selective CO₂ photoconversion, the selectivity towards CH₄ was summarized in Table S3. The oxygen-deficient Bi₂MoO₆ showed the higher CH₄ selectivity than BMO, and the most active BMO-OVs achieved the highest CH₄ selectivity of 96.7%. Besides the improved selective CH₄ evolution, the as-prepared BMO-OVs also exhibited good stability in recycling tests. In Fig. 4d, no obvious decrease of the CO or CH₄ production rate could be observed over BMO-OVs, even after the sixth run. It has been reported that photogenerated holes could oxidize H₂O to produce O₂ or O[•]H [48]. As demonstrated in Fig. S14, both BMO-OVs and BMO can oxidize H₂O to produce O[•]H, and the former demonstrated much higher [•]H generation ability, which is consistent with the CO₂ photoreduction activity. The wavelength dependent TCEN values of BMO-OVs and BMO were displayed in Fig. S15, revealing the correspondence of the photoactivity for CO₂ conversion with their absorption curve. A high TCEN of 0.9 was obtained at 420 nm for BMO-OVs, and it can work under the visible light region with a TCEN of 0.2 even at 500 nm, much higher than that of defect-free Bi₂MoO₆. Moreover, in order to figure out the origin of carbon atoms in reductive products, and exclude the disturbances of contaminated carbon during the synthesis, the isotopic experiment were carried out under a ¹³CO₂ atmosphere. As shown in

Fig. 4e, two strong total ion current peaks with retention time of 01'23" and 02'04" were detected and can be primarily assigned to the air and CO₂, respectively. The middle weak peak with retention time around 01'31" in the gas chromatogram can be indexed to the obtained CH₄, which presented a relatively high abundance of *m/z* = 17 (¹³CH₄). Together with the observed fragments of *m/z* = 16 (¹³CH₃) and *m/z* = 15 (¹³CH₂), it can be inferred that the produced ¹³CH₄ derived from ¹³CO₂ during the photocatalytic reduction process, which solidly proved that the CO₂ molecule are source of generated CH₄ rather than the residual surface carbons.

3.5. CO₂ methanation over BMO-OVs

The evaluation of photoelectrochemical properties can merely explain the enhanced activity, but the essential role of OVVs on selective CO₂ photoconversion remains to be unveiled. Therefore, temperature-programmed desorption (TPD) was performed to compare the CO₂ adsorption on BMO and BMO-OVs (Fig. 5a). CO₂-TPD spectra revealed that besides the two weak desorption peaks around 320 and 460 °C that were also found for BMO, an extra exceptionally high desorption peak at 232 °C was observed for BMO-OVs. Obviously, a new type of CO₂ adsorption appeared in oxygen-deficient BMO [49]. According to the theoretical calculations mentioned above, this can be assigned to the B1 type CO₂ adsorption that benefits the activation of CO₂ and promotes its conversion to ^{*}CHO and further hydrogenated to generate desired CH₄ [39]. Thereout, selective CO₂ photoreduction to CH₄ would occur. To experimentally verify the conjecture, in situ DRIFTS studies were operated in a special reaction cell to monitor the evolution of surfaced-bound species on BMO and BMO-OVs (Fig. 5b). The typical analysis was carried out in two sequential steps in a continuous-flow mode. First, CO₂ adsorption on the sample surface was studied by introducing a CO₂/H₂O mixture to the reaction cell at 30 °C for about 30 min in the dark till reaching saturation. Herein, the IR spectrum of the photocatalyst was collected as the background. Next, the Xe lamp was turned on for 60 min to investigate the photocatalytic conversion of reaction intermediates. It should be noted that in this step, the background was recollected after the saturated adsorption of CO₂/H₂O mixture.

Fig. 5c and d depicted the IR spectra of CO₂ and H₂O interaction

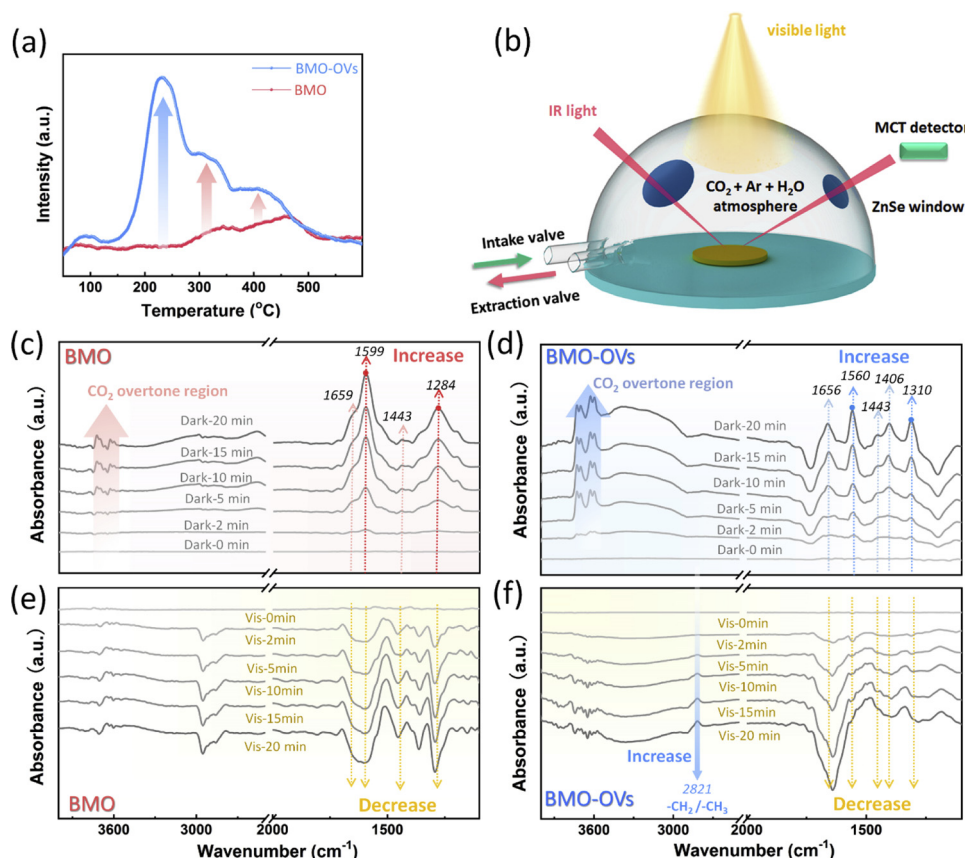


Fig. 5. (a) CO₂-TPD spectra for BMO-OVs and BMO; (b) Schematic illustration of the reaction cell for the *in situ* FTIR study; In situ DRIFTS tests of CO₂ and H₂O interaction with BMO and BMO-OVs (c, d) in the dark, and (e, f) subsequently irradiated by visible light.

with the catalysts prior to irradiation, from which significant differences can be easily observed between BMO and BMO-OVs. Differ from the two dominate peaks around 1599 and 1284 cm⁻¹ assigned to the bidentate carbonate (B2 type) adsorption on BMO [50–52], the bidentate carbonate peaks in BMO-OVs observably shifted to 1560 and 1310 cm⁻¹ [39,50,53]. In consistent with the previous theoretical calculation, this might result from the oxygen deficient structure of Bi₂MoO₆ with the formation of B1 type of CO₂ adsorption. Besides, multiple peaks also appeared more visibly for BMO-OVs around 3620, 2350, 1656, 1443, and 1406 cm⁻¹, which gradually raised over time with exposure to CO₂/H₂O. Based on previous literatures reports, the respective assignments of these various features are listed in Table S4. The visible broad adsorption peaks centered at around 2350 cm⁻¹ in Fig. S16 for both BMO and BMO-OVs are attributed to the ν_3 (CO₂) adsorption of gas-phase CO₂, accompanied with the appearance of weak overtone bands of gas-phase CO₂ around 3620 and 3725 cm⁻¹ [53]. Adsorption located at 1659 cm⁻¹ for BMO or 1656 cm⁻¹ for BMO-OVs is better assigned to the ν (CO=) mode of surface-bound *COOH or *CHO according to a previous *in situ* FTIR study on Titania nanotubes [53]. With respect to the weak adsorption peaks appeared at 1443 and 1406 cm⁻¹ over BMO-OVs, they can be assigned to the surface bi-carbonates which arise from the surface reaction of CO₂ and H₂O [50,53]. Additionally, surface-bound species evolution on the gas-saturated catalysts in visible light was respectively displayed in Fig. 5e and f, in which it should be noted that, for both BMO and BMO-OVs, all above mentioned peaks of CO₂ adsorbed species demonstrated significant negative growth immediately as light on. This implied the quick photoconversion of these species over the catalysts. Meanwhile, a new band at 2821 cm⁻¹ was observed to ratchet up with the irradiation time for BMO-OVs, which can be primarily ascribed to the ν_{as} (CH₂) vibration of surface *CH₂OH or *CH₃OH [22]. This evident surface

specie was not detected for pure BMO, indicating the hydrogenation of *CHO to CH₄ on BMO-OVs is more thermodynamically favorable than that on BMO. All these findings inferred that the different CO₂ adsorption on BMO-OVs (B1 type) critically changed the CO₂ conversion pathways and make it more easily converted into CH₄ under visible light irradiation. This is in high consistence with the theoretical calculations. In detail, well-designed OV on the prototypical {001} surface of Bi₂MoO₆ speak loudly in selective CH₄ evolution, since OVs can not only reform the photoelectrochemical properties of Bi₂MoO₆, but also favor the CO₂ adsorption in a possible special B1–CO₂ mode, which thermodynamically supports the further hydrogenation of intermediate CO* with the formation of *CHO. After series of subsequent hydrogenation steps, *CHO was finally converted into CH₄, realizing the high selective CO₂ photoreduction ultimately under the visible light irradiation.

4. Conclusion

In summary, the selective CO₂ photoconversion is achieved over defect-engineered Bi₂MoO₆ microspheres under visible light irradiation. Well-designed oxygen vacancies on the prototypical {001} surface of Bi₂MoO₆ can not only enhance light harvesting and e^-/h^+ separation, but also act as the natural active site for the CO₂ adsorption in a possible special bidentate carbonate mode, which thermodynamically supports the further hydrogenation of intermediate CO*. As a result, the CO and CH₄ formation rates achieved 0.27 and 2.01 $\mu\text{mol g}^{-1} \text{h}^{-1}$ over BMO-OVs, corresponding to the highest CH₄ selectivity of 96.7%. Based on the *in situ* DRIFTS analysis and calculated stepwise Gibbs free energy, the CO₂ adsorption species and reaction intermediates in the hydrogenation pathway were figured out, and a reasonable photocatalytic mechanism was proposed. This work reveals the important

roles of OV in selective CO₂ photoconversion, and can help us to design highly efficient CH₄ evolution systems.

Acknowledgments

This work was financially supported by National Natural Science Foundation of China (Nos. 51872107, 21607047, 21633004, 51902121 and 51572101), The World Premier International Research Center Initiative (WPI Initiative) on Materials Nanoarchitectonics (MANA), MEXT (Japan). National Basic Research Program of China (973 Program, No. 2014CB239301), Natural Science Foundation of Hubei Province (No. 2016CFB193) and Fundamental Research Funds for the Central Universities (Nos. 2662015QD047, 2662016PY088, 2662015QD011, 2015PY120 and 2015PY047).

Appendix A. Supplementary data

Supplementary material related to this article can be found, in the online version, at doi:<https://doi.org/10.1016/j.apcatb.2019.118088>.

References

- [1] A. Goeppert, M. Czaun, J.P. Jones, G.K. Surya Prakash, G.A. Olah, *Chem. Soc. Rev.* 43 (2014) 7995–8048.
- [2] J.L. White, M.F. Baruch, J.E. Pander III, Y. Hu, I.C. Fortmeyer, J.E. Park, T. Zhang, K. Liao, J. Gu, Y. Yan, T.W. Shaw, E. Abelev, A.B. Bocarsly, *Chem. Rev.* 115 (2015) 12888–12935.
- [3] N.S. Lewis, D.G. Nocera, *Proc. Natl. Acad. Sci. U. S. A.* 103 (2006) 15729–15735.
- [4] S. Xie, Q. Zhang, G. Liu, Y. Wang, *Chem. Commun.* 52 (2016) 35–59.
- [5] K. Li, B. Peng, T. Peng, *ACS Catal.* 6 (2016) 7485–7527.
- [6] W. Tu, Y. Zhou, Z. Zou, *Adv. Mater.* 26 (2014) 4607–4626.
- [7] S.N. Habisreutinger, L. Schmidt-Mende, J.K. Stolarczyk, *Angew. Chem. Int. Ed.* 52 (2013) 7372–7408.
- [8] N. Zhang, R. Ciriminna, M. Pagliaro, Y.J. Xu, *Chem. Soc. Rev.* 43 (2014) 5276–5287.
- [9] M. Zhou, S. Wang, P. Yang, C. Huang, X. Wang, *ACS Catal.* 8 (2018) 4928–4936.
- [10] X. Meng, G. Zuo, P. Zong, H. Pang, J. Ren, X. Zeng, S. Liu, Y. Shen, W. Zhou, J. Ye, *Appl. Catal. B: Environ.* 237 (2018) 68–73.
- [11] X. Chang, T. Wang, J. Gong, *Energy Environ. Sci.* 9 (2016) 2177–2196.
- [12] Y. Wang, F. Wang, Y. Chen, D. Zhang, B. Li, S. Kang, X. Li, L. Cui, *Appl. Catal. B: Environ.* 147 (2014) 602–609.
- [13] C. Dong, C. Lian, S. Hu, Z. Deng, J. Gong, M. Li, H. Liu, M. Xing, J. Zhang, *Nat. Commun.* 9 (2018) 1252.
- [14] G. Xi, S. Ouyang, P. Li, J. Ye, Q. Ma, N. Su, H. Bai, C. Wang, *Angew. Chem. Int. Ed.* 51 (2012) 2395–2399.
- [15] J. Wu, X. Li, W. Shi, P. Ling, Y. Sun, X. Jiao, S. Gao, L. Liang, J. Xu, W. Yan, C. Wang, Y. Xie, *Angew. Chem. Int. Ed.* 57 (2018) 8719–8723.
- [16] S. Xie, Y. Wang, Q. Zhang, W. Deng, Y. Wang, *ACS Catal.* 4 (2014) 3644–3653.
- [17] S. Bai, N. Zhang, C. Gao, Y. Xiong, *Nano Energy* 53 (2018) 296–336.
- [18] H. Li, J. Li, Z. Ai, F. Jia, L. Zhang, *Angew. Chem. Int. Ed.* 53 (2018) 122–138.
- [19] L. Liang, X. Li, Y. Sun, Y. Tan, X. Jiao, H. Ju, Z. Qi, J. Zhu, Y. Xie, *Joule* 2 (2018) 1004–1016.
- [20] X.Y. Kong, Y.Y. Choo, S.P. Chai, A.K. Soh, A.R. Mohamed, *Chem. Commun.* 52 (2016) 14242–14245.
- [21] H. Wang, D. Yong, S. Chen, S. Jiang, X. Zhang, W. Shao, Q. Zhang, W. Yan, B. Pan, Y. Xie, *J. Am. Chem. Soc.* 140 (2018) 1760–1766.
- [22] Z. Ma, P. Li, L. Ye, Y. Zhou, F. Su, C. Ding, H. Xie, Y. Bai, P.K. Wong, *J. Mater. Chem. A* 5 (2017) 24995–25004.
- [23] K. Zhao, L. Zhang, J. Wang, Q. Li, W. He, J.J. Yin, *J. Am. Chem. Soc.* 135 (2013) 15750–15753.
- [24] H. Li, J. Shang, Z. Ai, L. Zhang, *J. Am. Chem. Soc.* 137 (2015) 6393–6399.
- [25] S. Wang, X. Hai, X. Ding, K. Chang, Y. Xiang, X. Meng, Z. Yang, H. Chen, J. Ye, *Adv. Mater.* 29 (2017) 1701774.
- [26] J. Lee, D.C. Sorescu, X. Deng, *J. Am. Chem. Soc.* 133 (2011) 10066–10069.
- [27] Y. Pan, Z. Sun, H. Cong, Y. Men, S. Xin, J. Song, S. Yu, *Nano Res.* 9 (2016) 1689–1700.
- [28] J. Hou, S. Cao, Y. Wu, F. Liang, Y. Sun, Z. Lin, L. Sun, *Nano Energy* 32 (2017) 359–366.
- [29] J. Di, X. Zhao, C. Lian, M. Ji, J. Xia, J. Xiong, W. Zhou, X. Gao, Y. She, H. Liu, K.P. Loh, S.J. Pennycook, *Nano Energy* 61 (2019) 54–59.
- [30] M. Xing, Y. Zhou, C. Dong, L. Cai, L. Zeng, B. Shen, L. Pan, C. Dong, Y. Chai, J. Zhang, Y. Yin, *Nano Lett.* 18 (2018) 3384–3390.
- [31] X. Yang, Y. Xiang, Y. Qu, X. Ding, H. Chen, *J. Catal.* 345 (2017) 319–328.
- [32] Z. Dai, F. Qin, H. Zhao, J. Ding, Y. Liu, R. Chen, *ACS Catal.* 6 (2016) 3180–3192.
- [33] L. Ye, K. Deng, F. Xu, L. Tian, T. Peng, L. Zan, *Phys. Chem. Chem. Phys.* 14 (2012) 82–85.
- [34] Z. Nie, D. Ma, G. Fang, W. Chen, S. Huang, *J. Mater. Chem. A* 4 (2016) 2438–2444.
- [35] H. Li, J. Shang, Z. Yang, W. Shen, Z. Ai, L. Zhang, *Environ. Sci. Technol.* 51 (2017) 5685–5694.
- [36] X. Xu, X. Ding, X. Yang, P. Wang, S. Li, Z. Lu, H. Chen, *J. Hazard. Mater.* 364 (2019) 691–699.
- [37] W. He, Y. Sun, G. Jiang, Y. Li, X. Zhang, Y. Zhang, Y. Zhou, F. Dong, *Appl. Catal. B: Environ.* 239 (2018) 619–627.
- [38] S. Wang, X. Ding, X. Zhang, H. Pang, X. Hai, G. Zhan, W. Zhou, H. Song, L. Zhang, H. Chen, J. Ye, *Adv. Funct. Mater.* 27 (2017) 1703923.
- [39] L. Mino, G. Spoto, A.M. Ferrari, *J. Phys. Chem. C* 118 (2014) 25016–25026.
- [40] Y. Ji, Y. Luo, *J. Am. Chem. Soc.* 138 (2016) 15896–15902.
- [41] X. Nie, M. Esopi, M. Janik, A. Asthagiri, *Angew. Chem. Int. Ed.* 52 (2013) 2459–2462.
- [42] M. Cheng, E. Clark, H. Pham, A. Bell, M. Head-Gordon, *ACS Catal.* 6 (2016) 7769–7777.
- [43] Y. Zheng, T. Zhou, X. Zhao, W.K. Pang, H. Gao, S. Li, Z. Zhou, H. Liu, Z. Guo, *Adv. Mater.* (2017) 1700396.
- [44] C. Kongmark, R. Coulter, S. Cristol, A. Rubbens, C. Pirovano, A. Löfberg, G. Sankar, W. Beek, E. Bordes-Richard, R. Vannier, *Cryst. Growth Des.* 12 (2012) 5994–6003.
- [45] H. Li, J. Liu, W. Hou, N. Du, R. Zhang, X. Tao, *Appl. Catal. B: Environ.* 160–161 (2014) 89–97.
- [46] Z. Wei, Y. Liu, J. Wang, R. Zong, W. Yao, J. Wang, Y. Zhu, *Nanoscale* 7 (2015) 13943–13950.
- [47] Y. Bai, L. Ye, T. Chen, L. Wang, X. Shi, X. Zhang, D. Chen, *ACS Appl. Mater. Interfaces* 8 (2016) 27661–27668.
- [48] M.E. Aguirre, R. Zhou, A.J. Eugene, M.I. Guzman, M.A. Grela, *Appl. Catal. B: Environ.* 217 (2017) 485–493.
- [49] J. Mao, L. Ye, K. Li, X. Zhang, J. Liu, T. Peng, L. Zan, *Appl. Catal. B: Environ.* 144 (2014) 855–862.
- [50] W. Su, J. Zhang, Z. Feng, T. Chen, P. Ying, C. Li, *J. Phys. Chem. C* 112 (2008) 7710–7716.
- [51] L. Liu, Y. Jiang, H. Zhao, J. Chen, J. Cheng, K. Yang, Y. Li, *ACS Catal.* 6 (2016) 1097–1108.
- [52] L. Liu, H. Zhao, J.M. Andino, Y. Li, *ACS Catal.* 2 (2012) 1817–1828.
- [53] W. Wu, K. Bhattacharyya, K. Gray, E.J. Weitz, *J. Phys. Chem. C* 117 (2013) 20643–20655.